

Sonopermeation with Nanoparticle-Stabilized Microbubbles Reduces Solid Stress and Improves Nanomedicine Delivery to Tumors

Einar Sulheim,* Ingunn Hanson, Sofie Snipstad, Krister Vikedal, Yrr Mørch, Yves Boucher, and Catharina de Lange Davies

Drug delivery to tumors is challenging due to biological barriers obstructing effective delivery. Sonopermeation with ultrasound and microbubbles has been shown to improve therapeutic effect of many classes of drugs, but the underlying mechanism is not fully understood. In this study, two subcutaneous xenograft tumor models, that differed substantially in blood vessel density and stiffness, is treated with poly(alkyl cyanoacrylate) nanoparticles and nanoparticle-stabilized microbubbles combined with ultrasound. Improved nanoparticle accumulation and extracellular matrix (ECM) penetration is found. The stiffness and solid stress in the tumors are measured and it is discovered that sonopermeation can reduce the solid stress in both models, with the highest effect in the stiffest tumor model. This suggests that sonopermeation affects not only the blood vessel wall which has been described previously, but also the ECM to reduce solid stress and increase diffusion and transport of nanomedicines.

1. Introduction

Multiple biological barriers restrict drug delivery to solid tumors, particularly for macromolecules and nanomedicines.^[1–3] In order for the drug to reach the cellular compartment where most drugs find their target, several transport criteria must be fulfilled: 1) The tissue must be perfused to allow access for the drugs, 2) the drug must be able to cross the capillary wall, 3) the drug must penetrate the extracellular matrix (ECM), and 4) enter the cells. The use of macromolecules and nanomedicines to increase drug delivery selectively to tumors was described by multiple groups in the 80's^[4,5] and explained by the enhanced permeability and retention (EPR-) effect.^[6] As substantial research has been done and various nanomedicines have been approved for clinical use,^[7] it is clear that the EPR-effect

is a highly varying phenomenon^[8,9] and also the underlying mechanisms is a disputed question.^[10,11] Despite improving the tolerance and reducing systemic toxicity of the encapsulated pharmaceutical, several types of nanomedicines perform similarly to their free counterparts in terms of efficacy,^[12] indicating that the lack of success is hampered by the (tumor) biology. One of the least described, but important barrier is the stress that builds up in growing tumors,^[13] exerted by the cancer and stromal cells as well as collagen and hyaluronan in the interstitial matrix. This pressure can collapse blood vessels and restrict delivery of drugs and nanomedicines.^[14] Relieving this solid stress is thus a promising method to improve drug delivery to tumors.^[15]


Focused ultrasound (FUS) has in combination with ultrasound contrast agents (microbubbles, MBs) been used to achieve sonopermeation of solid tumors and metastases in the brain.^[16,17] Sonopermeation is described to open tight junctions and allow for penetration across the blood brain barrier^[18] and is used in multiple clinical trials^[19–21] (NCT03322813, NCT04146441, NCT03458975, NCT03477019, NCT04021420, NCT03385200, and NCT04021277). Furthermore, sonopermeation has also successfully improved the effect of gemcitabine in inoperable pancreatic patients.^[22] Preclinically, sonopermeation has been shown to have multiple interesting effects such as intercellular^[23] and intracellular^[24] pore formation, increased endocytosis^[25,26] and transcytosis,^[27] decreased P-glycoprotein

E. Sulheim, I. Hanson, S. Snipstad, K. Vikedal, C. de L. Davies
Department of Physics
Norwegian University of Science and Technology (NTNU)
Trondheim NO-7491, Norway
E-mail: einar.sulheim@ntnu.no

E. Sulheim, S. Snipstad, Y. Mørch
Department of Biotechnology and Nanomedicine
SINTEF AS
Trondheim 7034, Norway

E. Sulheim, S. Snipstad
Cancer Clinic
St.Olavs Hospital
Trondheim 7030, Norway

Y. Boucher
Edwin L. Steele Laboratory for Tumor Biology
Massachusetts General Hospital
Boston, MA 02114, USA

 The ORCID identification number(s) for the author(s) of this article can be found under <https://doi.org/10.1002/adtp.202100147>

© 2021 The Authors. *Advanced Therapeutics* published by Wiley-VCH GmbH. This is an open access article under the terms of the Creative Commons Attribution License, which permits use, distribution and reproduction in any medium, provided the original work is properly cited.

DOI: 10.1002/adtp.202100147

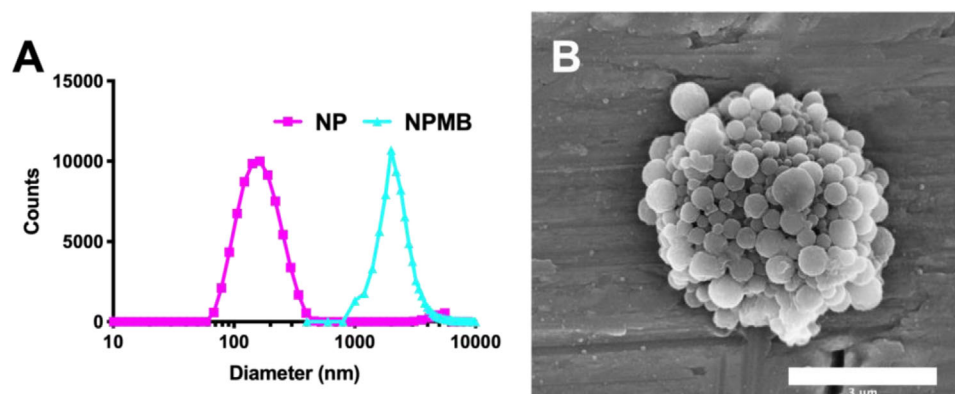


Figure 1. A) Size distribution of NPs, and NPMBs. B) SEM image of NP-stabilized MBs, scalebar 3 μm .

expression,^[28] decreased perfusion/vessel shutdown,^[29] but in other studies increased vascular perfusion.^[30,31] In sonopermeation, energy from the ultrasound wave is generally transferred to tissue through volumetric oscillations of MBs. As these MBs are confined to the vascular space, one could expect the biological effects to be confined to the vasculature. However, sonopermeation has also been reported to increase penetration of nanoparticles (NPs) through ECM^[32] and even improve delivery in the brain after intranasal delivery,^[33] neither of which can be explained easily by increased extravasation across the vessel wall.

The purpose of this study was to acquire fundamental knowledge of how sonopermeation can overcome biological barriers such as limited perfusion and dense ECM. These properties are both closely related to solid stress and relieving solid stress could likely improve both perfusion and ECM penetration.^[34] We approached this by treating two different tumor models that we characterized in detail in earlier work.^[35] Two main differences between the two tumor types are the extent of vascularization and the stiffness of the tumors. The prostate adenocarcinoma (PC3) xenograft is stiff and poorly vascularized especially in the central part of the tumor, whereas the osteosarcoma (OHS) xenograft is soft and well vascularized throughout the whole tumor. The tumors were treated with our in-house poly (alkyl cyanoacrylate) nanoparticle-stabilized microbubbles (NPMBs) and FUS. We have previously shown that these NPMBs in combination with FUS can improve the efficacy of cabazitaxel in a breast cancer model.^[36]

2. Results

The NPs produced had a Z-average diameter of 165 nm, a number average of 58 nm, polydispersity index of 0.23 and zeta potential of -2.8 mV. The bubbles had an average diameter of 2.3 μm and concentration of 6.4E8/mL (Figure 1).

The tumor accumulation of NPs was compared in the two tumor types with and without ultrasound (Figure 2). The PC3 tumors had a negligible EPR-effect with very low accumulation in control tumors compared to the control leg, but a significant effect of sonopermeation with a 2.5x increase in the fluorescence signal in sonopermeated tumors after 6 h. OHS tumors had a significant EPR effect (approximately doubled fluorescence signal compared to the PC3 tumors after 6 h), with 2x more fluores-

cence in the tumor leg compared to the contralateral leg after 6 h. The effect of sonopermeation was less pronounced than for PC3, but still significant, with an average of 1.5x greater accumulation of NPs in treated tumors compared to tumors that did not receive ultrasound. Note that there were three responders (i.e., having increased NP accumulation after sonopermeation) and three non-responders to the ultrasound exposure (Figure 2B) in the OHS group, whereas in the PC3 group all animals seemed to respond to ultrasound treatment. Interestingly, the absolute fluorescence in the two ultrasound-treated tumor groups was very similar, indicating that the ultrasound treatment had no synergy with the EPR-effect in OHS tumors.

To evaluate the intratumoral accumulation and penetration of NPs at a microscopic scale, we used confocal microscopy to assess the distribution of NPs in tumor sections (Figure 3A). Areas with functional blood vessels in the sections were observed in the FITC channel, and multichannel images showed also the NPs in areas with perfused blood vessels. Eight images were taken for each tumor section from three sections per tumor. This means that the NP accumulation reported is not the overall accumulation in the tumor, but rather the accumulation per functional blood vessel. Still, the accumulation in the various groups (Figure 3B) corresponded with the *in vivo* imaging results (Figure 2), but only a very modest (and not significant) effect of sonopermeation was observed in OHS tumors. In PC3 tumors the accumulation of NPs was 2x higher in the sonopermeated group. The functional blood vessels that were stained with FITC-lectin were used to evaluate the degree of extravasation and ECM penetration in the tumors. In compliance with the low EPR effect in PC3 tumors, it was found that OHS had a far higher degree of extravasation in untreated tumors with 80% of the NPs found in the images extravasated as compared to 50% for PC3 tumors (Figure 3C). Sonopermeation was able to significantly increase the extravasated fraction in PC3 tumors. Interestingly, in OHS the effect was opposite showing that sonopermeation is not necessarily beneficial for all tumor types. It was also found that most of these relatively large NPs accumulated close to blood vessels. Figure 3E shows the number of fluorescent pixels observed as a function of distance from the nearest blood vessel on a log₁₀ scaled Y-axis. While the slopes for both OHS groups and the FUS treated PC3 group were almost identical, a more negative slope was found in the non-treated PC3 group indicating that sonopermeation in

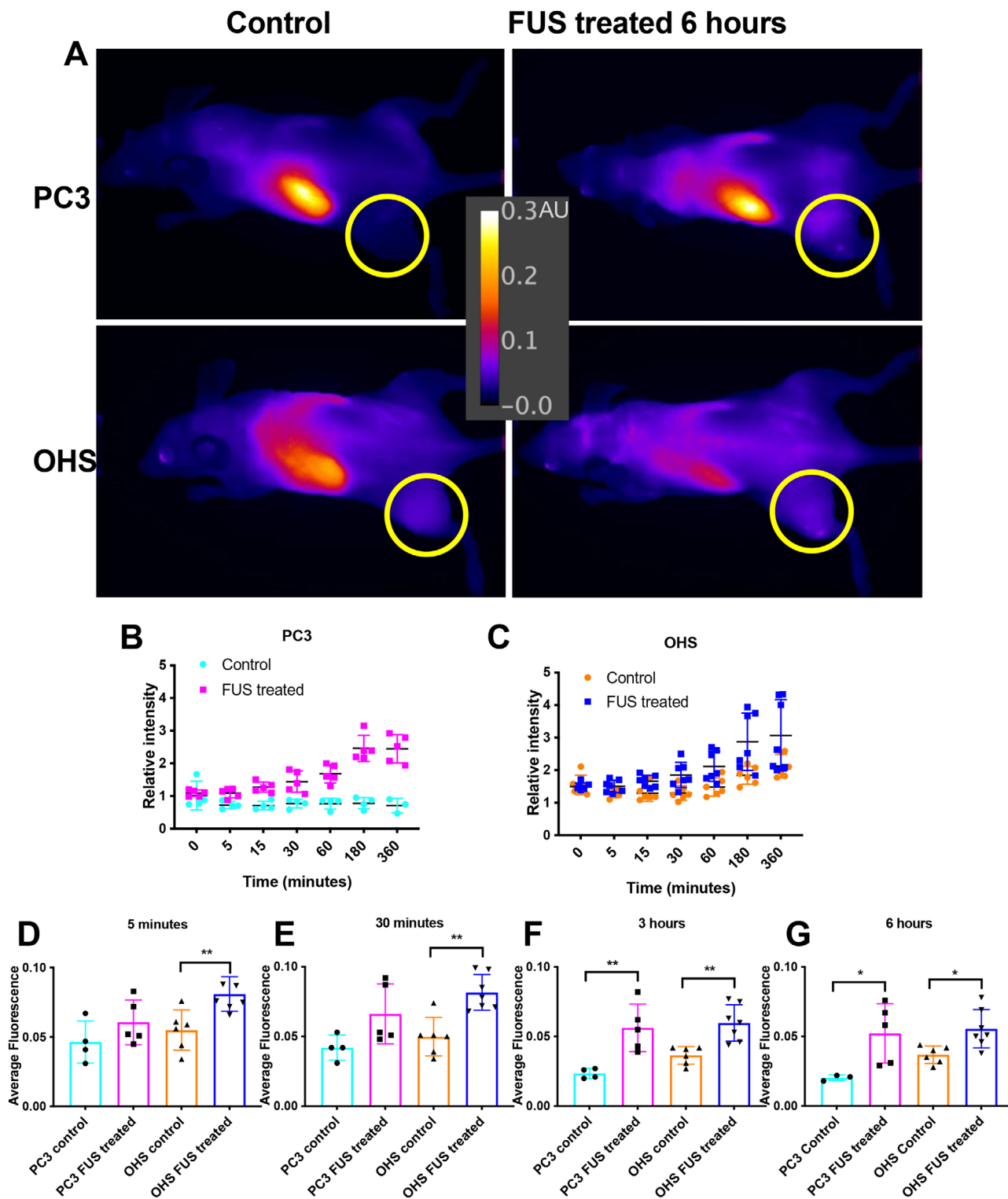
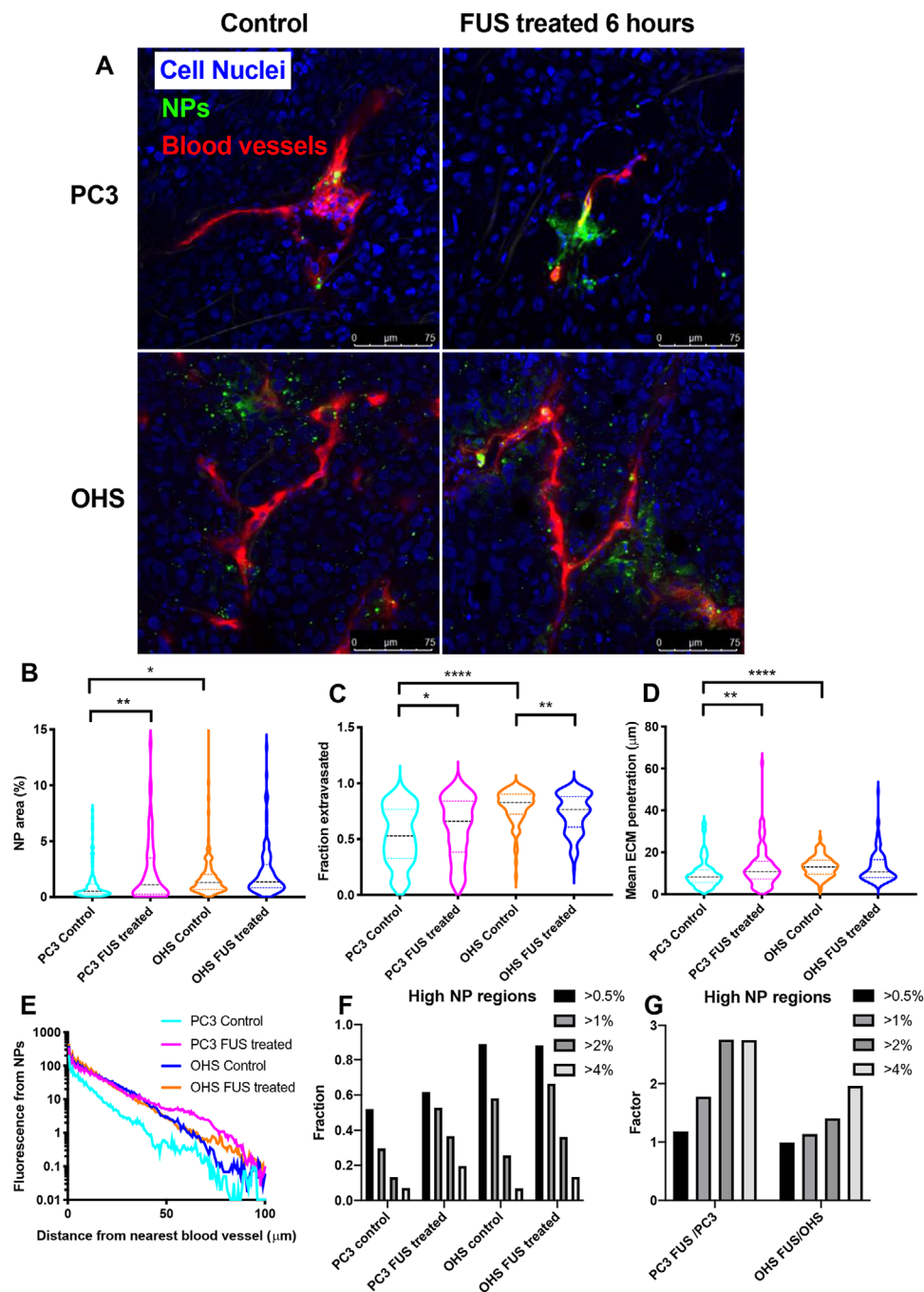


Figure 2. Effect of sonopermeation in PC3 and OHS tumors measured as the accumulation of IR780 loaded NPs. Controls are mice treated with the NP and NPMB mix, but without the FUS. A) Representative images of mice in the different groups 6 h after NP injection, the tumor on the hind leg is circled in yellow. The strong fluorescence is observed from the liver. B,C) The fluorescence signal from the tumor relative to an identical ROI on the right control leg without tumor, at timepoints from immediately after sonopermeation to 6 h post ultrasound. Average absolute fluorescence signal at D) 5 min, E) 30 min, F) 3 h, and G) 6 h post ultrasound. Each point represents one animal ($n = 4-7$ per group), error bars show standard deviation around the mean of each group and the groups were compared statistically with a two-tailed t-test.



this group can bring the ECM penetration depth up to the same level as for OHS tumors. This is also shown in Figure 3D giving the mean displacement in every group. It was found that sonopermeation could increase the mean penetration significantly, from 9.7 to 12.8 μm in PC3 tumors. The mean ECM penetration in OHS control and treated group were 13.0 and 12.9 μm , respectively. For the non-treated groups, it was found that the ECM penetration was significantly higher in OHS than PC3 tumors. To assess whether sonopermeation caused a general increase in the accumulation of NPs across the tumor or a large increase only in restricted regions, we counted the fraction of the images (regions of interest's (ROI's)) that had NP content above a certain threshold (0.5, 1, 2, and 4%) with and without sonopermeation. Figure 3F shows that for PC3 tumors, $\approx 50\%$ of the images have an NP fraction above 0.5% while in OHS more than 80% of the ROIs are above this threshold. Also for the 1% threshold, OHS shows a higher fraction of ROI's than PC3. However, for the higher thresholds (2% and 4%), PC3 have a higher fraction of the ROIs. This indicates that OHS has a more homogenous accumulation while the PC3 tumors have a subset of very leaky vessels. To better visualize the effect of sonopermeation Figure 3G shows the factor change from control to sonopermeation. We found that the fraction of ROIs above 0.5% is unchanged in both models, but for the high thresholds there is a clear effect of sonopermeation with a threefold change in PC3 and a twofold change in OHS.

To understand why the effect of sonopermeation differed in the two tumor models, we measured the stiffness of the tumor tissue using the planar cut method (Figure 4A), the displacement based on elevation of the tumor tissue and calculated the solid stress in the two tumor models with and without sonopermeation. As expected, PC3 were significantly stiffer than OHS tumors, but sonopermeation did not modify the stiffness in either models (Figure 4B). The groups (treated and untreated) were therefore combined to a joint group to get a Young's modulus to be used in the calculation of solid stress. The displacement was significantly higher in OHS than in PC3 tumors (Figure 4C), but the PC3 tumors were also significantly stiffer resulting in a similar solid stress in the two models (Figure 4D). We also found that the solid stress could be significantly reduced by sonopermeation in both models. The effect was strikingly similar in the two models with a 13.6% reduction in PC3 and a 13.1% reduction in OHS. Generally, higher solid stress was found toward the center of the tumor, but this was not without exceptions. High solid stress in the center was not because of necrotic regions as the both models exhibited very little necrosis. We compared NP delivery in low and high solid stress regions (Figure 4E) and found rather large variations and few significant differences, but the overall trend suggested higher NP accumulation in the low solid stress regions. For PC3 tumors the fraction of extravasated NPs was also slightly higher in the low solid stress region, while for OHS there was no apparent difference (Figure 4F). For all four groups, NPs penetrated further into the ECM in the low solid stress regions than in high solid stress regions (Figure 4G). In these low solid stress regions, there was a highly significant effect of sonopermeation on the ECM penetration in OHS tumors, while this effect was less pronounced in low solid stress regions in the PC3 tumors.

Following the observation of altered solid stress in the tumors after sonopermeation, we investigated the ECM in the two tumor

models and the state of the blood vessels. The distribution of collagen and hyaluronan for PC3 and OHS tumors are shown in Figure 5A,B, respectively. To evaluate the amount of functional vasculature, we stained vascular endothelial cells with CD-31 antibody and compared this staining to the vessels stained with lectin from the intravenous injection (functional vessels) (Figure 5C). We found that fibrillar collagen was present in both models, but significantly higher signal was measured in images from PC3 than OHS tumors (Figure 5D–F). Qualitatively, collagen was more evenly distributed throughout the tumor in PC3 tumors, while found less homogeneously distributed in OHS and a significant negative correlation was found between collagen content and number of functional vessels (Figure 5E). The amount of hyaluronan was similar in the two models (Figure 5G) and had no obvious effect on the vascular perfusion (Figure 5H). We found that OHS had the highest fraction of functional vessels (around 70% in both groups) while for PC3 the fraction was lower, and a reduction from sonopermeation was suggested although the difference was not significant ($p = 0.12$, Figure 5I). Reduction in the amount of functional vasculature has also been observed by others.^[37] There were no indications of altered amount of collagen or hyaluronan after treatment (Figure 5D,G). We also looked for lymphatic vessels by staining with LYVE-1, and such vessels were only found in the PC3 model (Figure 5C). The differences between the two tumor models are summarized in Table 1.

3. Discussion

The biological and biomechanical effects of sonopermeation are not fully understood. Sonopermeation can increase the delivery of small drugs and nanomedicines in both brain and solid tumors.^[16,38,39] However, the biological barriers are very different in these two scenarios^[40] and the observation that sonopermeation can be effective in both scenarios suggests that multiple effects can be obtained by ultrasound. In solid tumors which have chaotic, poorly functioning and leaky blood vasculature,^[41] blood vessel opening might be less important. A more important consequence of sonopermeation in solid tumors could be increased penetration through the tumor ECM^[42] that restricts the transport of drugs and macromolecules and creates solid stress.

In this study, we used a polymeric NP-MB system^[43] that has been shown effective in the treatment of tumors both as NPs only,^[44] and as MBs combined with FUS in the treatment of breast cancer^[36] and delivery across the blood brain barrier.^[45–47] We used two tumor models originating from human prostate (adenocarcinoma, PC3) and bone (OHS) that have in our previous studies been found to be very different in terms of vasculature and NP accumulation.^[35] We found that sonopermeation increased NP delivery in both PC3 and OHS tumors. PC3 showed the strongest benefit from sonopermeation with more extravasation and deeper penetration of NPs into the ECM observed in sonopermeated tumors. When the accumulation was assessed not by the entire tumor, but by selecting ROI's with perfused blood vessels, the effect of much higher vascular fraction in OHS^[35] is removed. In this situation the accumulation in the sonopermeated PC3 tumors and both OHS groups are very similar, while the untreated PC3 tumors have significantly lower accumulation. This shows that the apparently higher EPR effect in the OHS tumors does not necessarily correspond to more leaky

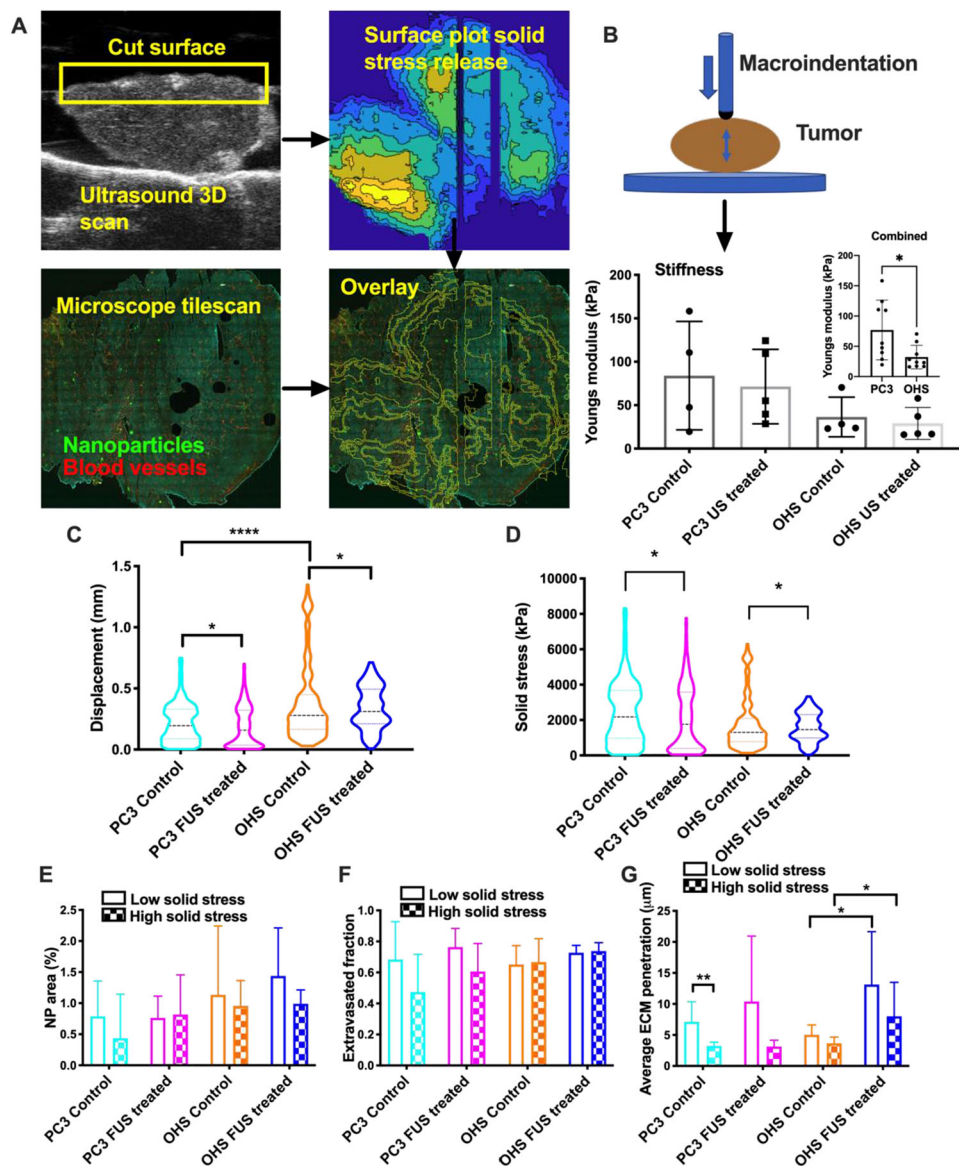


Figure 4. Measurement of solid stress and the effect of solid stress on NP distribution. A) Image maps showing the measurement of solid stress induced displacement and overlay with tile scans from microscopy. The upper left panel shows the ultrasound image of the tumor surface after relaxation and elevation of tissue, right panel shows the surface plot of the height in the cutting plane and the corresponding tumor area as a tile scan. The lower left panel shows the tile scan of the tumor section and the lower right panel shows an overlay of the surface map (yellow lines) with the tile scan. In the height map, yellow areas show the regions with the highest displacement, whereas blue areas show the lowest elevation. In the microscope tile scan, green shows NPs, blue shows cell nuclei and red shows blood vessels. B) The stiffness/Young's modulus of the tumors measured with a macroindenter. C) The mean displacement and D) Released solid stress (calculated as relative displacement multiplied by Young's modulus) after cutting the tumor in two. Each datapoint is the mean tissue elevation in the ultrasound images of the tumors (40–60 images/tumor). E) Area fraction of NPs in low and high solid stress regions. F) Extravasated fraction of NPs in low and high solid stress areas. G) ECM penetration of NPs in the low and high solid stress regions. The bars in (E–G) show mean of 4–5 tumors per group and 24 images per tumor quantified as in Figure 3. The groups were compared pairwise with a two-tailed Welch t-test.

blood vessels but is rather a cumulative effect from the higher number of blood vessels, and that the sonopermeation of PC3 tumors was only able to increase the accumulation per blood vessel up to the same level as in OHS tumors. These observations indicate that the main effect sonopermeation has on delivery is not by increasing the number of NP-delivering blood vessels, but rather to improve the delivery in those that are already functional

and supports the idea that the microbubbles can only have effects in the relative proximity to where they are sonified, which is in a functional blood vessel.

While accumulation per blood vessel is relatively similar in the two sonopermeated tumor types, the effect on extravasation is diverging. In PC3 tumors sonopermeation significantly increases the fraction of NP found outside blood vessels and increased the

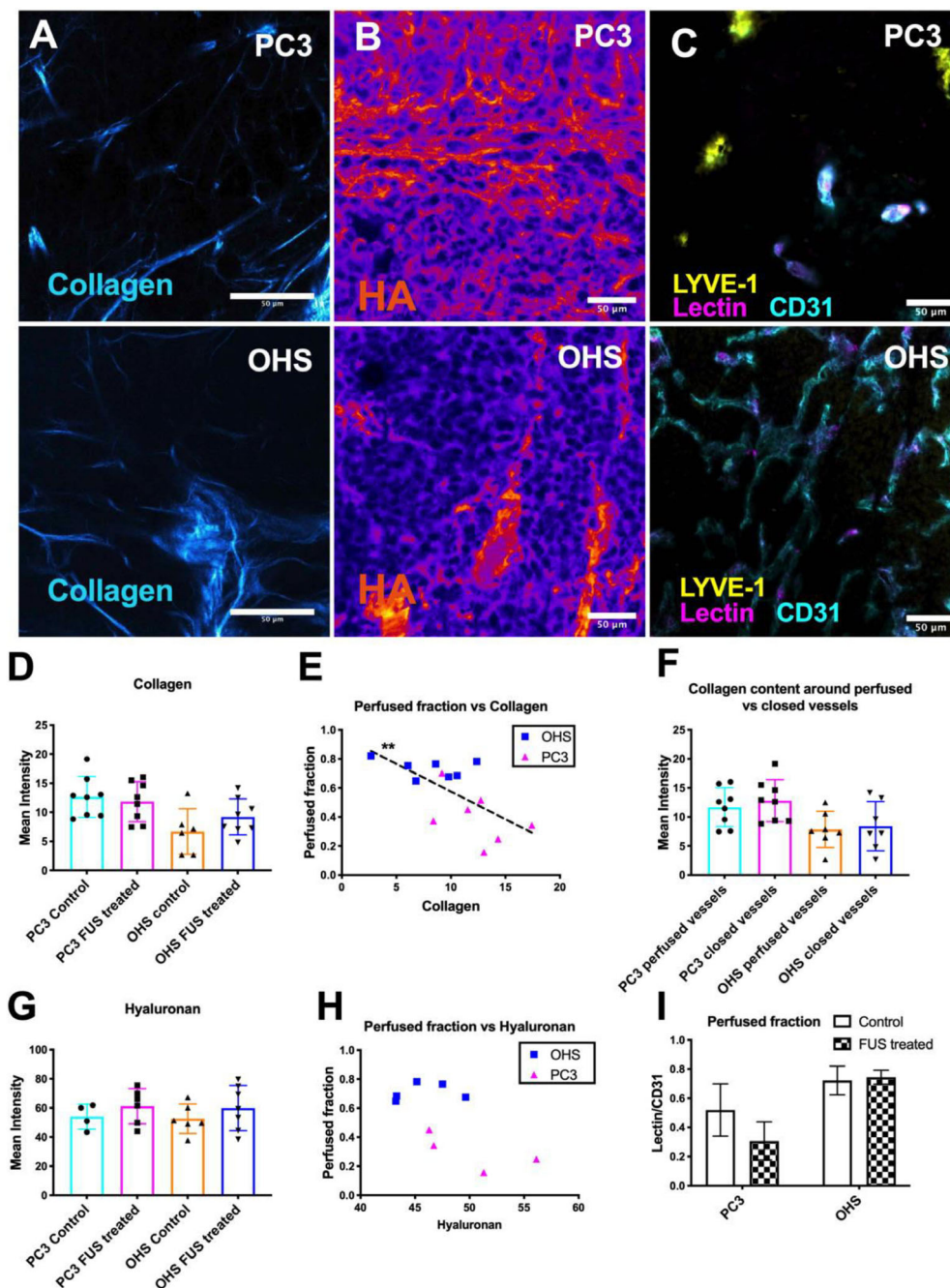


Figure 5. ECM components and blood vessels in the tumor models. Representative images show A) collagen, B) hyaluronan (heatmap), and C) blood vessels and lymphatic veins in the two tumor models. D) Amount of collagen, 2 sections from each of 4 tumors were analyzed from each group. E) Correlation between collagen content and perfused vascular fraction in the tumors. The line shows a linear fit with $R^2 = 0.44$ and asterisks mark significance level with Pearson correlation, 5 tumors of each type. F) Collagen content in regions with perfused and non-perfused blood vessels. G) Amount of hyaluronan, 1 section from 5 tumors of each type was analyzed. H) Perfused fraction versus hyaluronan content in the tumors. I) Fraction of perfused vessels in the treatment groups.

average penetration of NP into the extracellular compartment, these changes were not observed in OHS tumors. Also, the ECM penetration of NPs in PC3 was increased up to the level of OHS. Together this shows that sonopermeation impacts both extravasation and penetration of NPs.^[32] There are no indications that the

altered perfusion pattern is the main reason because most of the observed increase can be explained by increase per blood vessel, and the increased accumulation of NP is created by a large increase in the accumulation around a subset of the blood vessels in particular for PC3 tumors. This also shows that the effect of

Table 1. Differences between the PC3 and OHS tumor models. “High” and “low” describes a relative difference between the two models.

Tumor model	PC3	OHS
EPR-effect	Low	High
Effect from sonopermeation	High	Low
Vessel density ^[35]	Low	High
Solid stress induced displacement	Low	High
Stiffness	High	Low
Solid stress	High	Low
Cell density ^[35]	Low	High
Collagen density	High	Low
Lymphatic density	High	Low
Perfused vascular fraction	Low	High
Hyaluronan density	Medium	Medium

sonopermeation depends heavily on properties of the tumor tissue such as ECM constituents and the quality and functionality of the blood vessels.

It has previously been shown that solid stress in tumors can close lymphatic vessels as well as blood vessels and reduce the overall perfusion,^[14,48] and drugs that reduce solid stress have been shown to increase both the delivery and penetration of nanomedicines.^[14,49] We measured the solid stress in both models and found surprisingly that sonopermeation could reduce the solid stress by 13% in both tumor models, which is to our knowledge never reported previously. Our results suggest that the solid stress hinders transport of NPs through ECM and is a barrier for extravasation in the stiffest model (PC3). This is in coherence with other studies using drugs such as losartan,^[14] but reduced solid stress and increased drug delivery by ultrasound was not achieved by the same mechanism as for pharmacological treatment. Decreased solid stress is in these cases observed by a reduction in cancer-associated fibroblasts, an increase in perfused fraction of blood vessels^[34] and often a reduction in collagen and hyaluronan density.^[14] We observed neither of those, but hypothesize that the effect from sonopermeation must be related to the ECM as only the solid compartment of the tumors can create the solid stress.^[50] In our experiments, solid stress is measured 1 h after ultrasound hence the change occurs during or immediately after sonopermeation. It is therefore unlikely that observation comes from a reduction in ECM components as this would require more time. Consistent with this, we did not observe any change in the amount of either collagen or hyaluronan. It has previously been shown that sonopermeation can have extravascular effects by acting as a pump that transfers energy into the ECM by “massaging” the blood vessels wall causing vibrations in the perivascular space.^[51,52] In these studies, the effect of sonopermeation was seen to last beyond the treatment time as increased delivery was seen also when the drug was given after the ultrasound treatment was finished. Our hypothesis is that the vibration reorganizes ECM components such as collagen and hyaluronan in the proximity of blood vessels causing improved transport properties and reduced solid stress. However, such potential reorganization could not be detected by the optical imaging methods applied here. We consider the observation of better

effect of sonopermeation in the stiffer model to support or hypothesis.

The two tumor models are different in multiple aspects (Table 1) and the difference in effect from sonopermeation could originate from multiple of these. In another comparable study, Theek et al. measured the accumulation and penetration of liposomes in two low-EPR tumor models after sonopermeation.^[32] The results in the two tumor models were relatively similar in their case, even though the tumor models differed significantly both in cell density and collagen content. Interestingly, and in coherence with our study and the notion that sonopermeation has extravascular effects, Theek et al. observed increased liposome delivery in regions 30–50 μm away from blood vessels after sonopermeation. Similarly, in a study using liposomes in the PC3 model, our group has previously observed increased penetration in a distance up to 60 μm from blood vessels.^[53] Similar penetration distance was observed here and shows that the increased penetration is not merely an effect of increased NP accumulation, but rather that the NPs are pushed deeper into the tissue showing that sonopermeation has consequences also at a distance from the blood vessel wall. In OHS tumors, increased extravasation distance was not observed, both treated and untreated tumors showed comparable NP extravasation as the PC3 group. The OHS tumors have very low stiffness and are highly flexible suggesting a less rigid ECM that might be a less important barrier than in stiffer models such as PC3. The higher Youngs modulus/stiffness found in PC3 tumors corresponds well to the higher amount of collagen and the observed stiffness by manual palpation.

Our results point in the direction of (at least) two separate effects giving improved drug delivery by sonopermeation. The first would be the most conventional, where MBs vibrate and collapse in proximity to the blood vessel wall giving increased permeability/extravasation in functional blood vessels, as seen especially in blood brain barrier opening, but also in the PC3 tumor model. The other effect would be ECM reorganization, increasing the penetration through ECM,^[54] which could possibly explain the effect of sonopermeation after intranasal delivery^[51] and reduced solid stress. A secondary effect of reduced solid stress could be vascular opening and increased perfusion which has been reported in several preclinical studies^[30,31] and could explain the increased effect of gemcitabine in the clinical study of pancreatic cancer.^[22,30]

Our study shows that sonopermeation is a promising method for drug delivery to tumors, but that patient stratification and understanding of the biological barriers in different cancer types is crucial. We show that FUS in combination with MBs can help overcome barriers of drug transport, not only the barrier of the blood vessel wall, but also the ECM outside the blood vessels. However, further studies are needed to fully understand the underlying mechanisms. In our view sonopermeation is a promising strategy for cancer therapy that could potentially increase the efficacy of many of the drugs in clinical practice today.

4. Experimental Section

Nanoparticles and Microbubbles Synthesis and Characterization: The NPs and MBs consist of both free NPs and NP-stabilized MBs in the same mixture. The product is made by first synthesizing poly(alkyl cyanoacrylate)

NPs and in a second step mixing the NPs with hydrophobic gas and protein to form MBs where $\approx 1\%$ of the NPs are found on the MB surface, the remaining 99% free in solution.^[43]

The NPs were made in a one-step miniemulsion synthesis as described^[43] and characterized for PEGylation and circulation time,^[55] payload stability,^[56] degradation,^[57] and toxicity^[58] in previous work. In this study the NPs were made of 2-ethyl-butyl cyanoacrylate (Cuantum) loaded with both the visible dye NR668^[59] (synthesized by SINTEF) and the near infrared dye IR780-lipid^[60] (synthesized by CEA Grenoble). The oil phase in the miniemulsion consisted of 0.25wt% of the two dyes, 2.25 g 2-ethyl butyl cyanoacrylate and stabilizers (5wt% Miglyol 812, Cremer and 5wt% vanillin, Sigma-Aldrich). The water phase consisted of PEG-surfactants (6wt% Brij L23, 23 PEG units, MW 1225 and 6wt% Kolliphor HS15, 15 PEG units, MW 960, Sigma-Aldrich) in 18 mL 0.1 M HCl. The miniemulsion was formed by sonicating for 3 min on ice (6×30 s intervals, 60% amplitude, Branson Ultrasonics digital sonifier 450). Polymerization was carried out overnight at ambient temperatures before pH was adjusted to 5 and polymerization continued for 5 h. The NPs were finally dialyzed against 1 mM HCl to remove excess surfactant. The NPs were characterized for size and zeta potential in phosphate buffer (pH 7.4, 0.01 M) with dynamic light scattering (Zetasizer nano ZS, Malvern).

MBs were formed by mixing NPs and casein (Sigma-Aldrich) to a final concentration of 0.5 and 1wt%, respectively (pH 7) using an ultra turax (Branson Ultrasonics) in a perfluoropropane (F2 Chemicals) saturated environment.^[43] Microbubbles were characterized for size and concentration by microscopy (Olympus) in a countess cell counting chamber slide (ThermoFisher) and analysis in image, as well as, and imaged by scanning electron microscopy (SEM, Hitachi S-5500).

Cells and Animals: Human prostate adenocarcinoma cells (PC3, ATCC) were cultivated in Dulbecco's Modified Eagles Medium (Gibco) and human OHS cells^[61] in Rosa Park Memorial Institute (RPMI, Gibco) medium, both supplemented with 10% fetal bovine serum (Sigma-Aldrich). Cells were maintained at 37 °C with 5% CO₂ in exponential growth phase. Before inoculation, the cells were detached by trypsin (Sigma-Aldrich), counted using a Countess automated cell counter (ThermoFisher) and resuspended in cell medium containing 1% penicillin/streptomycin at a concentration of 60 millions mL⁻¹.

Female Balb/c nude mice (Janvier) were bought at 8 weeks of age and housed in specific pathogen free conditions at 22–23 °C and 50–60% relative humidity with free access to food and water. All animal procedures were approved by the Norwegian Animal Research Authorities under FOTS# 14 872.

For inoculation of tumor cells, the animals were anesthetized with isoflurane in O₂ and NO₂ (Baxter). 3 million cells in 50 μ L cell medium were inoculated subcutaneously on the left hind leg. The animals were then inspected twice weekly for weight, tumor size, and behavior. No animals exhibited weight loss or signs of pain due to the tumor growth. Experiments were initiated as the tumors reached 8–10 mm in the longest axis, that is, volume of ≈ 250 mm³.

Ultrasound Exposure: For FUS treatment and subsequent imaging, animals were anesthetized with a subcutaneous injection of fentanyl (0.05 mg kg⁻¹, Actavis Group), medetomidine (0.5 mg kg⁻¹, Orion Pharma), midazolam (5 mg kg⁻¹, Accord Healthcare Limited), and water (2:1:2:5) at a dose of 0.1 mL per 10 g. The animals were then placed on top of a water tank with an ultrasound absorbing plate, and the left hind leg with the tumor was pulled through a hole in the plate and into the water. Immediately before FUS treatment, 100 μ L of the NP and NPMB mix was administered intravenously through the tail vein. Ultrasound was given from a custom-made setup with a single element 1 MHz transducer (Imasonic). The signal was generated by a waveform generator (33 500 B, Agilent Technologies), and amplified with 50 dB power amplifier (2100 L, E&I). The tumors were treated with a pressure of 0.5 MPa resulting in a mechanical index (MI) of 0.5, bursts of 10 000 cycles at a local pulse repetition frequency (PRF) of 10 Hz for 0.5 s, followed by a 1.5 s break to allow for reperfusion with microbubbles, giving a global PRF of 0.5 Hz and a total duty cycle of 2.5%. This was continued for 2 min. The setup and treatment settings were optimized and are described in more detail in previous work.^[36] Con-

rol animals were positioned in the same setup and given the same NPMB injection but with the ultrasound off.

Whole Animal Optical Imaging and Analysis: Following the FUS treatment the animals were imaged in a small animal optical imaging system (Pearl Impulse, LI-COR Biosciences) at timepoints (post treatment, in minutes); 0, 5, 15, 30, 60, 180, 360, before the animals were euthanized and tumors removed. This was done to characterize accumulation of NPs in the tumors, for both tumor types 4–7 animals were included in the groups (control and sonopermeation). Excitation/emission settings were 785 nm/820 nm. ROIs were made on the tumor leg and on the control leg without a tumor to compare the mean intensity NPs using imageJ. Both the fluorescence value relative to an equal ROI on the opposite leg, and the absolute values are presented. 5 min before euthanasia, 100 μ L FITC lectin (diluted in saline to 1 mg mL⁻¹, Vector Labs) was injected through the tail vein.

Solid Stress Measurements: For solid stress measurements, the animals were euthanized 60 min after FUS treatment. For both tumor types 4–5 animals were used as untreated controls and 4–5 animals were treated with FUS. 5 min before the animals were euthanized, 100 μ L FITC-lectin was injected intravenously through the catheter in the tail vein. Solid stress was measured by the planar cut method as described by Nia et al.^[62] based on solid-stress induced deformation and stiffness of the tumor. After excision the tumor was embedded in 2% agarose (Sigma-Aldrich) gel that was solidified on ice. The tumor and agarose gel were then manually cut in two equal hemispheres with a scalpel along the center of the tumor at an axis parallel to the thighbone. The cutting plane was then imaged by high-resolution ultrasound (Vevo 2100, 40 MHz transducer, VisualSonics) using a 3D step motor (step length 63,5 μ m, VisualSonics) to capture cross section-images equally spaced across each tumor. Using the agarose gel on both sides of the tumor as reference, the elevation of the tumor tissue was measured on ultrasound images using Fiji and MatLab, and this value is denoted as solid-stress induced displacement. For analysis every third image was used resulting in a distance of 190 μ m between the analyzed images and 40–70 images for each tumor. Images were manually inspected for artifacts such as gas bubbles and removed from analysis. The tumors were then covered in a drop of OCT Tissue Tec (Sakura), frozen in liquid N₂ and cut in 25 μ m sections. The sections were mounted with Vectashield with DAPI and the entire section was imaged using tile scanning with a Zeiss Axio microscope with a 20x/0.5 air objective. DAPI was excited at 405 nm and detected at 400–520 nm, FITC was excited at 488 nm and detected at 410–545 nm and NR668 was excited at 561 nm and detected at 553–627 nm. To compare the accumulation of NPs in the regions of differing solid stress, the area with displacement from 0 to 277 μ m was defined as low solid stress while areas with displacement >556 μ m was defined as high solid stress regions.

Solid stress was calculated as relative displacement (solid stress induced displacement/tumor radius) * Youngs modulus.

$$S = E \times \Delta L/R \quad (1)$$

where E = Youngs modulus and $\Delta L/R$ = Relative displacement (solid stress induced displacement/tumor radius.)

Stiffness Measurement: Stiffness was measured on a separate set of tumors, 4–5 in each group using a macroindenter (custom setup). The tumors were compressed at a constant rate of 2 μ m s⁻¹ for 200–400 μ m. The linear part of the weight/time curve was used to calculate Young's modulus E using the formula from herzian mechanics:^[63]

$$F = \frac{4}{3} \frac{E}{(1 - \nu^2)} R^{\frac{1}{2}} D^{\frac{3}{2}} \quad (2)$$

where F is the indentation force, D is indentation depth, ν is the poisson ratio. ν was assumed to be 0.4 for both tumors based on literature.^[64,65] $R = 2,25$ mm is the radius of the circular indenter. Because no significant difference in stiffness was found between the treated and untreated tumors, the two groups were merged and the average Youngs modulus of each tumor type was used for the calculation of solid stress. An average diameter of 7 mm was used for all tumors.

Antibody Staining: Antibody staining was done on the same tumors that were used for solid stress measurements; the mice were euthanized 60 min after ultrasound treatment. Blood vessels were labelled by staining the sections with an antibody for mouse CD-31 (mCD-31 (PECAM-1), BD Biosciences) at a 1:100 dilution. The CD-31 antibody was visualized by a Cy3 labelled anti-rat antibody (Dianova) at a 1:500 dilution. Hyaluronan was labelled with a biotinylated hyaluronan-binding protein (Millipore) at a concentration of 16 µg mL and visualized with an AMCA-labelled streptavidin at 1:200 dilution (Dianova). Prior to staining with the hyaluronan binding protein endogenous biotin was blocked using an Avidin/Biotin blocking kit (Dako). Lymphatic vessels were labelled with LYVE-1 antibody (Abcam) at a 1:100 dilution and visualized by an AMCA-labelled anti-rabbit antibody (Dianova) at 1:50 dilution. Staining protocols for all cases were as follows: Sections were washed in PBS for 2 min and fixed in cold 80% MeOH for 5 min and cold acetone for 2 min followed by another washing in PBS for 5 min. The sections were then permeabilized in 0.1% Triton X-100 for 10 min before washing in PBS for 5 min. The sections were then stained with the primary antibody diluted in 12% BSA for 1 h at room temperature, washed three times with PBS (5 min each) and incubated for 45 min at room temperature with the secondary antibody. Finally, the sections were washed three times in PBS (5 min each) and mounted with Vectashield (Vector Labs) and a cover glass. All chemicals were from Sigma-Aldrich unless stated specifically.

Microscopy: NP uptake and extravasation was measured in sections from tumors in mice sacrificed 6 h after sonopermeation. Sections with NPs and lectin staining (stains only the functional blood vessels) were mounted with Vectashield mounting medium and a cover slip and imaged with a Leica SP8 confocal microscope using a 40x/1.1 water objective. NR668 in the NPs was excited at 561 nm and detected at 570–613 nm. FITC-lectin was excited at 501 nm and detected at 510–560 nm, both were excited using a white laser and detected on HyD detectors. Three sections spaced >1 mm apart were analyzed with 8 images from each section for a total of 24 images per tumor.

Antibody-stained sections were imaged on a Zeiss Axio with a 20x/0.8 air objective. CD-31 staining was imaged by excitation at 561 nm and detecting emission at 400–700 nm, FITC-lectin was imaged by excitation at 488 nm and emission at 410–545 nm, LYVE-1 and hyaluronan were imaged by excitation at 405 nm and emission at 405–545 nm, all with a filter blocking the excitation wavelength.

The second harmonic generation signal from fibrous collagen was acquired with a Leica SP8 microscope with a 63x/1.20 water objective. The sections were illuminated by a multiphoton laser at $\lambda = 780$ nm and emitted light was detected in an external Hyd detector at 370–410 nm. For each tumor Section 16 images were acquired by finding 8 perfused (signal in both lectin and CD-31 channel) vessels and 8 non-perfused (signal in CD-31 channel only) blood vessels and imaging the collagen in the same field of view.

Image Analysis: Image analysis was performed in Fiji. For quantification of NP accumulation, images were thresholded both in the FITC and NR668 channels using the triangle algorithm in Fiji. The various thresholding algorithms were manually evaluated on a representative set of images and triangle was considered most accurate. NP accumulation was defined as the ratio of colored pixels in the thresholded, binary image. To calculate the number of NPs as a function of distance from the blood vessels, the binary blood vessel image was used to create a distance map using the Fiji feature. The binary image from the NR668 channel was then overlaid on the distance map and used to separate the NPs into regions of different values in the distance map.

For solid stress measurements, the ultrasound images of the tumor surface were thresholded using the IsoData algorithm in Fiji after manually comparing the accuracy of the different thresholding options. The “zero” level was then manually defined by making a straight line between the tumor-gel intersections and a 2D surface vector was made by measuring the number of pixels in the thresholded image above the “zero” line. This was done on 40–70 images per tumor and combined to make a 3D surface map of the tumor. The surface map was then overlaid the tile scan of the tumor section and used to calculate the NP accumulation in regions of differing solid stress.

Collagen and HA was quantified by summarized the pixel intensities in the images. CD-31 and lectin-stained blood vessels were compared by manually counting the number of blood vessels in the two channels in randomly chosen ROIs.

Statistics: Statistical analysis was performed in Prism 8 (Graphpad). Groups are compared using a t-test unless otherwise stated, significant *p*-values are denoted as * < 0.05, ** < 0.01, *** < 0.001.

Acknowledgements

Anne Rein Hatletveit at SINTEF Biotechnology and Nanomedicine is acknowledged for synthesizing nanoparticles and microbubbles. Stein Martin Fagerland is acknowledged for help setting up the ultrasound imaging. Astrid Bjørkøy is acknowledged for advice on microscopy and stiffness measurements. Ida Marie Høiaas is acknowledged for help in acquiring SEM images. Housing and care of animals were provided by the Comparative Medicine Core Facility (CoMed), and tissue sections were prepared by the Cellular and Molecular Imaging Core Facility (CMIC), both at NTNU. Imaging was performed at the Center for Advanced Microscopy (CAM) at NTNU. The project was funded by the Central Norway Regional Health Authorities (grant number 46084000) and the Research Council of Norway, project number 262228.

Conflict of Interest

The authors declare no conflict of interest.

Data Availability Statement

Research data are not shared.

Keywords

cancer, drug delivery, nanomedicine, sonopermeation, ultrasound

Received: June 23, 2021
Published online: July 28, 2021

- [1] R. K. Jain, *Cancer Res.* **1990**, *50*, S814.
- [2] R. K. Jain, T. Stylianopoulos, *Nat. Rev. Clin. Oncol.* **2010**, *7*, 653.
- [3] S. K. Sriraman, B. Aryasomayajula, V. P. Torchilin, *Tissue Barriers* **2014**, *2*, e29528.
- [4] R. K. Jain, L. T. Baxter, *Cancer Res.* **1988**, *48*, 7022.
- [5] Y. Matsumura, H. Maeda, *Cancer Res.* **1986**, *46*, 6387.
- [6] H. Maeda, J. Wu, T. Sawa, Y. Matsumura, K. Hori, *J. Controlled Release* **2000**, *65*, 271.
- [7] C. Von Roemeling, W. Jiang, C. K. Chan, I. L. Weissman, B. Y. S. Kim, *Trends Biotechnol.* **2017**, *35*, 159.
- [8] A. E. Hansen, A. L. Petersen, J. R. Henriksen, B. Boerresen, P. Rasmussen, D. R. Elema, P. M. A. f. Rosenschöld, A. T. Kristensen, A. Kjær, T. L. Andresen, *ACS Nano* **2015**, *9*, 6985.
- [9] H. Lee, A. F. Shields, B. A. Siegel, K. D. Miller, I. Krop, C. X. Ma, P. M. Lorusso, P. N. Munster, K. Campbell, D. F. Gaddy, S. C. Leonard, E. Geretti, S. J. Blocker, D. B. Kirpotin, V. Moyo, T. J. Wickham, B. S. Hendriks, *Clin. Cancer Res.* **2017**, *23*, 4190.
- [10] S. Sindhwani, A. M. Syed, J. Ngai, B. R. Kingston, L. Maiorino, J. Rothschild, P. Macmillan, Y. Zhang, N. U. Rajesh, T. Hoang, J. L. Y. Wu, S. Wilhelm, A. Zilman, S. Gadde, A. Sulaiman, B. Ouyang, Z. Lin, L. Wang, M. Egeblad, W. C. W. Chan, *Nat. Mater.* **2020**, *19*, 566.

- [11] T. Skotland, K. Sandvig, *Nano Today* **2020**, *36*, 101029.
- [12] S. Wilhelm, A. J. Tavares, Q. Dai, S. Ohta, J. Audet, H. F. Dvorak, W. C. W. Chan, *Nat. Rev. Mater.* **2016**, *1*, 16014.
- [13] R. K. Jain, J. D. Martin, T. Stylianopoulos, *Annu. Rev. Biomed. Eng.* **2014**, *16*, 321.
- [14] V. P. Chauhan, J. D. Martin, H. Liu, D. A. Lacorre, S. R. Jain, S. V. Kozin, T. Stylianopoulos, A. S. Mousa, X. Han, P. Adstamongkonkul, Z. Popović, P. Huang, M. G. Bawendi, Y. Boucher, R. K. Jain, *Nat. Commun.* **2013**, *4*, 2516.
- [15] V. Kumar, Y. Boucher, H. Liu, D. Ferreira, J. Hooker, C. Catana, A. J. Hoover, T. Ritter, R. K. Jain, A. R. Guimaraes, *Transl. Oncol.* **2016**, *9*, 431.
- [16] S. Snipstad, E. Sulheim, C. d. L. Davies, C. Moonen, G. Storm, F. Kiessling, R. Schmid, T. Lammers, *Expert Opin. Drug Delivery* **2018**, *15*, 1249.
- [17] S. Snipstad, Y. Mørch, E. Sulheim, A. Åslund, A. Pedersen, C. d. L. Davies, R. Hansen, S. Berg, *Ultrasound Med. Biol.* **2021**, *47*, 1319.
- [18] C. Poon, D. McMahon, K. Hynynen, *Neuropharmacology* **2017**, *120*, 20.
- [19] A. Carpentier, M. Canney, A. Vignot, V. Reina, K. Beccaria, C. Horodyckid, C. Karachi, D. Leclercq, C. Lafon, J.-Y. Chapelon, L. Capelle, P. Cornu, M. Sanson, K. Hoang-Xuan, J.-Y. Delattre, A. Idhah, *Sci. Transl. Med.* **2016**, *8*, 343re2.
- [20] Y. Wang, Y. Li, K. Yan, L. Shen, W. Yang, J. Gong, K. Ding, *Chin. J. Cancer Res.* **2018**, *30*, 553.
- [21] A. Idhah, M. Canney, L. Belin, C. Desseaux, A. Vignot, G. Bouchoux, N. Asquier, B. Law-Ye, D. Leclercq, A. Bissery, Y. De Rycke, C. Troesch, L. Capelle, M. Sanson, K. Hoang-Xuan, C. Dehais, C. Houillier, F. Laigle-Donadey, B. Mathon, A. André, C. Lafon, J.-Y. Chapelon, J.-Y. Delattre, A. Carpentier, *Clin. Cancer Res.* **2019**, *25*, 3793.
- [22] G. Dimcevski, S. Kotopoulos, T. Bjånes, D. Hoem, J. Schjøtt, B. T. Gjertsen, M. Biermann, A. Molven, H. Sorbye, E. Mccormack, M. Postema, O. H. Gilja, *J. Controlled Release* **2016**, *243*, 172.
- [23] N. Sheikov, N. Mcdannold, S. Sharma, K. Hynynen, *Ultrasound Med. Biol.* **2008**, *34*, 1093.
- [24] I. Skachkov, Y. Luan, A. F. van der Steen, N. de Jong, K. Kooiman, *IEEE Trans. Ultrason., Ferroelectr. Freq. Control* **2014**, *61*, 1661.
- [25] B. D. M. Meijering, L. J. M. Juffermans, A. Van Wamel, R. H. Henning, I. S. Zuhorn, M. Emmer, A. M. G. Versteilen, W. J. Paulus, W. H. Van Gilst, K. Kooiman, N. De Jong, R. J. P. Musters, L. E. Deelman, O. Kamp, *Circ. Res.* **2009**, *104*, 679.
- [26] M. Afadzi, S. P. Strand, E. A. Nilssen, S.-E. Masoy, T. F. Johansen, R. Hansen, B. A. Angelsen, C. D. L. Davies, *IEEE Trans. Ultrason., Ferroelectr. Freq. Control* **2013**, *60*, 21.
- [27] N. Sheikov, N. Mcdannold, F. Jolesz, Y.-Z. Zhang, K. Tam, K. Hynynen, *Ultrasound Med. Biol.* **2006**, *32*, 1399.
- [28] M. Aryal, K. Fischer, C. Gentile, S. Gitto, Y.-Z. Zhang, N. Mcdannold, *PLoS One* **2017**, *12*, e0166061.
- [29] X. Hu, A. Kheirrolomoom, L. M. Mahakian, J. R. Beegle, D. E. Kruse, K. S. Lam, K. W. Ferrara, *Invest. Radiol.* **2012**, *47*, 398.
- [30] A. Rix, M. Palmowski, F. Gremse, K. Palmowski, W. Lederle, F. Kiessling, J. Bzyl, *Ultrasound Med. Biol.* **2014**, *40*, 2468.
- [31] J. T. Belcik, B. H. Mott, A. Xie, Y. Zhao, S. Kim, N. J. Lindner, A. Ammi, J. M. Linden, J. R. Lindner, *Circ.: Cardiovasc. Imaging* **2015**, *8*, e002979.
- [32] B. Theek, M. Baues, T. Ojha, D. Möckel, S. K. Veetil, J. Steitz, L. Van Bloois, G. Storm, F. Kiessling, T. Lammers, *J. Controlled Release* **2016**, *231*, 77.
- [33] D. Ye, X. Zhang, Y. Yue, R. Raliya, P. Biswas, S. Taylor, Y.-C. Tai, J. B. Rubin, Y. Liu, H. Chen, *J. Controlled Release* **2018**, *286*, 145.
- [34] T. Stylianopoulos, J. D. Martin, V. P. Chauhan, S. R. Jain, B. Diop-Frimpong, N. Bardeesy, B. L. Smith, C. R. Ferrone, F. J. Hornicek, Y. Boucher, L. L. Munn, R. K. Jain, *Proc. Natl. Acad. Sci. USA* **2012**, *109*, 15101.
- [35] E. Sulheim, J. Kim, A. Van Wamel, E. Kim, S. Snipstad, I. Vidic, I. H. Grimstad, M. Widerøe, S. H. Torp, S. Lundgren, D. J. Waxman, C. D. L. Davies, *J. Controlled Release* **2018**, *279*, 292.
- [36] S. Snipstad, S. Berg, Y. Mørch, A. Bjørkøy, E. Sulheim, R. Hansen, I. Grimstad, A. Van Wamel, A. F. Maaland, S. H. Torp, C. D. L. Davies, *Ultrasound Med. Biol.* **2017**, *43*, 2651.
- [37] A. K. Wood, S. Ansaloni, L. S. Ziemer, W. M. Lee, M. D. Feldman, C. M. Sehgal, *Ultrasound Med. Biol.* **2005**, *31*, 1403.
- [38] J. Park, M. Aryal, N. Vykhodtseva, Y.-Z. Zhang, N. Mcdannold, *J. Controlled Release* **2017**, *250*, 77.
- [39] A. V. Wamel, A. Healey, P. C. Sontum, S. Kvåle, N. Bush, J. Bamber, C. D. L. Davies, *J. Controlled Release* **2016**, *224*, 158.
- [40] A. Pluen, Y. Boucher, S. Ramanujan, T. D. Mckee, T. Gohongi, E. Di Tomaso, E. B. Brown, Y. Izumi, R. B. Campbell, D. A. Berk, R. K. Jain, *Proc. Natl. Acad. Sci. USA* **2001**, *98*, 4628.
- [41] N. K. Reitan, M. Thuen, P. E. Goa, C. D. L. Davies, *J. Biomed. Opt.* **2010**, *15*, 036004.
- [42] K. C. Valkenburg, A. E. De Groot, K. J. Pienta, *Nat. Rev. Clin. Oncol.* **2018**, *15*, 366.
- [43] Y. Mørch, R. Hansen, S. Berg, A. K. O. Åslund, W. R. Glomm, S. Eggen, R. Schmid, H. Johnsen, S. Kubowicz, S. Snipstad, E. Sulheim, S. Hak, G. Singh, B. H. Mcdonagh, H. Blom, C. D. L. Davies, P. M. Stenstad, *Contrast Media Mol. Imaging* **2015**, *10*, 356.
- [44] M. Fusser, A. Øverbye, A. D. Pandya, Y. Mørch, S. E. Borgos, W. Kildal, S. Snipstad, E. Sulheim, K. G. Fleten, H. A. Askautrud, O. Enggebraaten, K. Flatmark, T. G. Iversen, K. Sandvig, T. Skotland, G. M. Mælandsmo, *J. Controlled Release* **2018**, *293*, 183.
- [45] H. Baghirov, S. Snipstad, E. Sulheim, S. Berg, R. Hansen, F. Thorsen, Y. Mørch, C. D. L. Davies, A. K. O. Åslund, *PLoS One* **2018**, *13*, e0191102.
- [46] A. K. O. Åslund, S. Berg, S. Hak, Y. Mørch, S. H. Torp, A. Sandvig, M. Widerøe, R. Hansen, C. D. L. Davies, *J. Controlled Release* **2015**, *220*, 287.
- [47] E. Sulheim, Y. Mørch, S. Snipstad, S. E. Borgos, H. Miletic, R. Bjerkvig, C. D. L. Davies, A. K. O. Åslund, *Nanotheranostics* **2019**, *3*, 103.
- [48] T. P. Padera, B. R. Stoll, J. B. Tooredman, D. Capen, E. D. Tomaso, R. K. Jain, *Nature* **2004**, *427*, 695.
- [49] F. Mpekris, P. Papageorgis, C. Polydorou, C. Voutouri, M. Kalli, A. P. Pirentis, T. Stylianopoulos, *J. Controlled Release* **2017**, *261*, 105.
- [50] V. P. Chauhan, Y. Boucher, C. R. Ferrone, S. Roberge, J. D. Martin, T. Stylianopoulos, N. Bardeesy, R. A. Depinho, T. P. Padera, L. L. Munn, R. K. Jain, *Cancer Cell* **2014**, *26*, 14.
- [51] H. Chen, G. Z. X. Yang, H. Getachew, C. Acosta, C. S. Sánchez, E. E. Konofagou, *Sci. Rep.* **2016**, *6*, 28599.
- [52] H. Chen, W. Kreider, A. A. Brayman, M. R. Bailey, T. J. Matula, *Phys. Rev. Lett.* **2011**, *106*, 034301.
- [53] M. Olsman, V. Sereti, K. Andreassen, S. Snipstad, A. Van Wamel, R. Eliassen, S. Berg, A. J. Urquhart, T. L. Andresen, C. D. L. Davies, *J. Controlled Release* **2020**, *325*, 121.
- [54] C. D. Arvanitis, V. Askoxylakis, Y. Guo, M. Datta, J. Kloepper, G. B. Ferraro, M. O. Bernabeu, D. Fukumura, N. Mcdannold, R. K. Jain, *Proc. Natl. Acad. Sci. USA* **2018**, *115*, E8717.
- [55] A. K. O. Åslund, E. Sulheim, S. Snipstad, E. von Haartman, H. Baghirov, N. Starr, M. K. Løvmo, S. Lelú, D. Scurr, C. L. Davies, R. Schmid, Y. Mørch, *Mol. Pharming* **2017**, *14*, 2560.
- [56] S. Snipstad, S. Hak, H. Baghirov, E. Sulheim, Y. Mørch, S. Lélú, E. von Haartman, M. Bäck, K. P. R. Nilsson, A. S. Klymchenko, C. d. L. Davies, A. K. O. Åslund, *Cytometry A* **2016**, *91*, 760.
- [57] E. Sulheim, H. Baghirov, E. Von Haartman, A. Bøe, A. K. O. Åslund, Y. Mørch, C. D. L. Davies, *J. Nanobiotechnol.* **2016**, *14*, 1.

- [58] E. Sulheim, T.-G. Iversen, V. T. Nakstad, G. Klinkenberg, H. Sletta, R. Schmid, A. Hatletveit, A. Wågbo, A. Sundan, T. Skotland, K. Sandvig, Ý. Mørch, *Int. J. Mol. Sci.* **2017**, *18*, 2454.
- [59] A. S. Klymchenko, E. Roger, N. Anton, H. Anton, I. Shulov, J. Vermot, Y. Mely, T. F. Vandamme, *RSC Adv.* **2012**, *2*, 11876.
- [60] A. Jacquart, M. Kéramidas, J. Vollaie, R. Boisgard, G. Pottier, E. Rustique, F. Mittler, F. P. Navarro, J. Boutet, J.-L. Coll, I. Texier, *J. Biomed. Opt.* **2013**, *18*, 101311.
- [61] Ø. Fodstad, A. Brøgger, Ø. Bruland, O. P. Solheim, J. M. Nesland, A. Pihl, *Int. J. Cancer* **1986**, *38*, 33.
- [62] H. T. Nia, H. Liu, G. Seano, M. Datta, D. Jones, N. Rahbari, J. Incio, V. P. Chauhan, K. Jung, J. D. Martin, V. Askoxylakis, T. P. Padera, D. Fukumura, Y. Boucher, F. J. Hornicek, A. J. Grodzinsky, J. W. Baish, L. L. Munn, R. K. Jain, *Nat. Biomed. Eng.* **2017**, *1*, 0004.
- [63] X. Li, Y. H. An, Y.-D. Wu, Y. C. Song, Y. J. Chao, C.-H. Chien, *J. Biomed. Mater. Res., Part B* **2007**, *80*, 25.
- [64] M. T. Islam, R. Righetti, *Comput. Biol. Med.* **2019**, *111*, 103343.
- [65] M. T. Islam, S. Tang, C. Liverani, S. Saha, E. Tasciotti, R. Righetti, *Sci. Rep.* **2020**, *10*, 7266.